Noise requirements of the cryogenic shielding for next generation cryocooled gravitational wave observatories: Newtonian noise

Edgard Bonilla,[1,*] Brett Shapiro,[1] Brian Lantz,[1] Odylio Denys Aguiar,[2] and Marcio Constancio[2]
[1]*Stanford University, Stanford, California 94305, USA*
[2]*Instituto Nacional de Pesquisas Espaciais, Divisão de Astrofísica, S. J. Campos, São Paulo 12227, Brazil*

(Received 9 September 2021; accepted 19 October 2021; published 23 December 2021)

We explore the vibration isolation requirements imposed by Newtonian noise on the cryogenic shielding for next-generation gravitational-wave observatories relying on radiative cooling. Two sources of Newtonian noise from the shield arrays are analyzed: the tidal coupling from the motion of a shield segment to its nearby test mass's displacement, and the effect of density fluctuations due to heterogeneous boiling of cryogenic liquids in the vicinity of the test masses. It was determined that the outer shields require no additional vibration isolation from ground motion to mitigate the Newtonian noise coupling to levels compatible with the LIGO Voyager design. Additionally, it was determined that the use of boiling nitrogen as the heat sink for the cryogenic arrays is unlikely to create enough Newtonian noise to compromise the detector performance for either Voyager or Cosmic Explorer phase 2. However, the inherent periodicity of the nucleation cycle might acoustically excite structural modes of the cryogenic array which could contaminate the signals from the interferometer through other means. This last effect could be circumvented by using a single-phase coolant to absorb the heat from the cryogenic shields.

DOI: 10.1103/PhysRevD.104.122005

I. INTRODUCTION

The first direct detection of gravitational waves by the Advanced LIGO Observatories in 2015 [1] kicked off the new field of gravitational-wave astronomy. Additionally, the first observation of gravitational waves produced by a neutron star-neutron star merger [2] opened a new window in our understanding of the Universe through multimessenger astronomy [3].

With the success of the LIGO and Virgo observatories, there is much interest in further improving the technologies that make gravitational-wave detection possible. Multiple upgrades have been proposed [4–6] to maximize the detection capabilities of the existing infrastructure. Similarly, projects for so-called third-generation detectors are currently in their design phase [7–9].

These proposals incorporate different combinations of changes to the current technology, including longer baselines, heavier test masses, changes in the circulating power, and cryogenic temperatures. All of these have the potential to mitigate the fundamental sources of noise for the interferometers.

This set of papers focuses on detectors that combine the use of 124 K silicon test masses[1] and high circulating power in the interferometer cavities.[2] These features are shared by LIGO Voyager [5] and the second stage of Cosmic Explorer (CE2) [8].

The operating temperature of 124 K enables the exclusive use of radiative coupling to a 'cryogenic shield' to hold the temperature of the test masses inside the vacuum chamber. Radiation-only cooling is advantageous from a vibration isolation perspective because the closest common mechanical connection between the test masses and the cooling equipment is the ground.[3] However, the high circulating power in the cavity imposes stringent isolation requirements for objects in the vicinity of the test mass that could reflect scattered light back to the main beam.[4] It then becomes necessary to use a vibration-isolated double cryogenic shield like the one proposed and tested in [12]. This double-shield design is adopted in the plans for LIGO Voyager [5].

Much of the cryogenic technology is still in the design and prototype phase. The design for the cryogenic shields

*edgard@stanford.edu

[1]The choice of material and operating temperature are driven by a reduction of thermoelastic noise. Silicon's thermal expansion coefficient crosses zero around 124 K [10].

[2]Increasing the laser power is one way to reduce shot noise.

[3]One alternative is to use ribbons to conduct the heat from the test masses, as done by KAGRA [11]. Their operating temperature of 20 K prevents the use of radiation as the only mechanism of heat absorption for the test masses. In their case, the closest common mechanical connection between the cooling equipment and the test masses is only a few stages of passive isolation away from the test mass.

[4]The scattered-light noise requirements for cryogenic shields are the subject of part two in this set of articles.

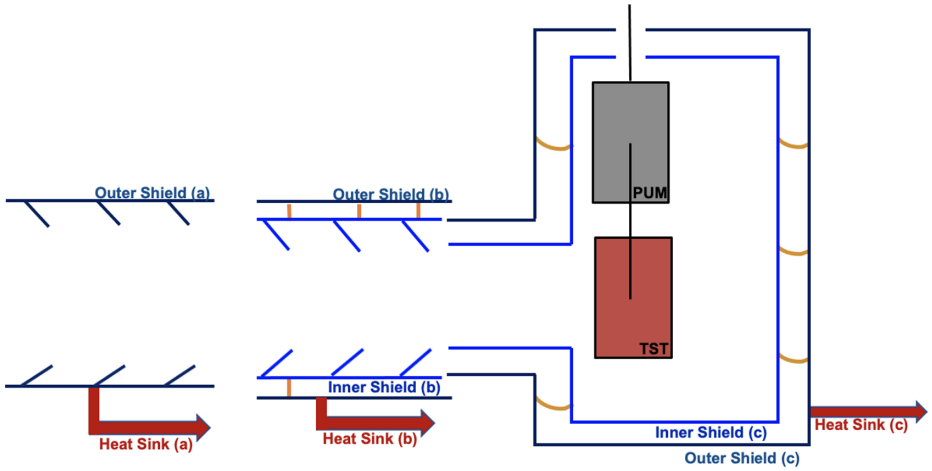

FIG. 1. Diagram for an end-test-mass (ETM) double-layer cryogenic shield array. The array encompasses three regions around the test mass and the beam tube. The outer shield segments are connected to a heat sink outside the vacuum wall and are not seismically isolated. The inner shield segments are connected by flexible heat links to the outer shield and are both suspended and actively controlled for vibration isolation. In this diagram, both the test mass (TST) and the penultimate mass (PUM) are included inside the shields.

will have to simultaneously satisfy the vibration isolation, vacuum, and heat removal requirements for steady-state operation of the observatories. A fully functional prototype of a suspended Fabry-Perot cavity operating at 124 K with steady-state radiative cooling has not yet been demonstrated.

This paper is the first of a set of two articles exploring the vibration isolation requirements of the cryogenic shields. The purpose of these articles is to lay out calculations and estimates necessary to inform the design decisions for the cryogenics of third-generation gravitational-wave detectors, as well as to provide justification for the conceptual diagrams presented in [5,12] in the specific case of LIGO Voyager. This paper focuses on the requirements set by Newtonian noise coupling to the longitudinal motion of the test masses. This noise coupling sets the isolation requirements for the outermost layer of the cryogenic shields. Part two will deal with the more stringent isolation requirements imposed on the inner layer of cryogenic shielding by scattered light noise coupling.

Most Newtonian noise studies focus on seismic and atmospheric fields [13,14], but it is well known that other disturbances near test masses like vibrating structures or flowing water can potentially lead to significant gravitational coupling [15,16]. However, to the authors' knowledge, this is the first article providing estimates for this type of coupling in the context of equipment immediately surrounding the test masses.

The body of this document is structured as follows. In Sec. II, we provide the background for the calculations, including a general overview of the double cryogenic shield design and Newtonian noise coupling. In Sec. III we lay out the calculations to estimate the Newtonian noise arising from the relative motion of the cryogenic shields and the test masses. In Sec. IV we explore the Newtonian noise from rapid density changes in boiling liquids near the test masses. In Sec. V we apply our calculations to the context of the design of the cryogenic shields for LIGO Voyager, which allows us to derive a set of design considerations and constraints for this specific project. We include results that are relevant to the second stage of Cosmic Explorer when appropriate.

II. LITERATURE BACKGROUND

A. Double cryogenic shields

A sketch of the geometry of a double cryogenic shield is shown in Fig. 1, based on the design ideas proposed in [12]. In it, two shields, which we dub the inner shield and the outer shield, surround the test mass and reaction mass/compensation plate of the interferometers, as well as parts of the beam tubes. Each shield is divided into independent segments: one in the portion between two gate valves connecting the test mass's vacuum chamber to the main beam pipe, a second one covering the beam path leading to the test mass, and the last one surrounding the test mass itself. These segments are labeled (a), (b), and (c), respectively, in Fig. 1.

All outer shield segments are connected to cooling plants outside of the vacuum chamber by a heat sink. This connection could in principle be a heat pipe, a simple metal rod or liquid nitrogen plumbing. This heat sink is responsible for absorbing the heat load of the inner shield and the radiation from the surrounding vacuum chamber during cooldown and operation of the interferometer.

The inner shield segments are all suspended for passive isolation and need to be actively isolated to mitigate scattered light coupling.[5] The inner shield segments are

[5]This will be further elaborated on in part 2 of this set of articles.

connected to the outer shield through a compliant connection (such as copper braid).

The input test masses and end test masses (ITMs and ETMs, respectively) will likely have two different shield geometries due to their different position and function in the interferometer arms. The ITM shields will have two open snouts to leave the beam path uninterrupted, while the ETM shields will have a window past the test mass, mounted on the outer shield.

Additionally, for the purposes of reducing thermal noise coupling, it has been considered that the cryogenic shields should include the penultimate mass of the suspension chain, in addition to the test mass. We will consider both configurations in our examples for this article.

Figure 1 also shows that all the shield segments must be connected to an appropriate heat sink mechanism to transfer their heat load to a cryocooler located outside the vacuum chamber. This connection can be made, for example, through a metal rod, a heat pipe or a flowing liquid cryogen. The choice of mechanism will ultimately depend on a tradeoff between cost, noise injection to the interferometer, and ability to perform both in the initial cooldown and as a steady-state heat sink.

In this article, we consider the situation where the heat is carried away from the shields through flow boiling of liquid nitrogen. This option has the advantage of being both inexpensive and capable of high power absorption, but not much has been said about its potential contribution to the noise of the interferometers. We will study the potential Newtonian noise generated by the evaporation process as the liquid nitrogen boils near the test masses.

B. Newtonian noise

The term Newtonian noise is used to describe the fluctuations in the gravitational field surrounding the test masses that both originates from local sources, and is completely explainable by Newtonian gravity.

In the case of the cryogenic shields, there are two main mechanisms capable of generating Newtonian noise: First, the tidal forces induced by the motion of the shields around the test mass. Second, the density fluctuations in the liquid coolant, caused by the phase transition, as it boils near the test mass.

The exact couplings of these two sources of Newtonian noise to the gravitational-wave channel depend strongly on the geometry of the shields. For that reason, we will limit ourselves to deriving upper bounds and order of magnitude assessments of their impact. We believe these estimates will be enough to set limits and help drive the discussion about the specific design of the cryogenic shields.

We will begin our calculations by considering the gravitational coupling between a point mass and a uniform cylindrical mass (which represents the test mass). Then, we will show how to extend this result to the continuous body of the cryogenic shields to estimate the tidal Newtonian noise from the shields. Finally, the point-mass model will be used to estimate the potential effect of moving bubbles of gaseous nitrogen in the cryogenic array.

C. Acceleration between a point mass and a cylinder

The gravitational force between a point mass and a uniform cylinder is investigated in [17]. From this work, we extract an expression for the axial acceleration per-unit-mass $\alpha_x(r,\theta)$ that a point mass exerts on a uniform cylinder,[6]

$$\alpha_x(r,\theta) = G\sum_{n=0}^{\infty}\left[\frac{P_{2n+1}(\cos(\theta))}{r^2}\left(\frac{l}{r}\right)^{2n} \times \sum_{k=0}^{n} C[2n+1,2k]\frac{P_{2k}(0)}{k+1}\left(\frac{b}{l}\right)^{2k}\right], \quad (1)$$

where G is the universal gravitational constant, r represents the distance between the point mass and the center of mass of the cylinder, and θ is the angle measured from the axis of symmetry of the cylinder. Additionally, l is the half thickness of the cylinder and b is its radius. $C[n,k]$ is the binomial coefficient 'n choose k'. Finally, $P_k(x)$ represents the kth Legendre polynomial.

III. TIDAL NEWTONIAN NOISE

The Newtonian coupling of the shield arrays to each of the test masses' axial forces will be driven both by their rigid-body motion and their internal, structural modes of vibration. To give a conservative estimate for the total Newtonian noise coupling, we can study separate components of the shields individually, adding their contributions either in absolute value (if they are correlated) or in quadrature (if they are uncorrelated).

For simplicity, consider a single continuous component of the cryogenic shields,[7] together with the test mass closest to it. Let us assume we separate this shield portion $\mathcal{S}$ into several infinitesimal mass elements $dm = dm(\vec{r}')$, indexed by their positions $\vec{r}'$ in the shield. Let $\delta\vec{r}(\vec{r}',t)$ represent the vector field of displacements of the mass elements dm of this shield portion with respect to their equilibrium positions. The net contribution of the motion of the shield to its corresponding test mass's axial acceleration is given by

$$\delta a_x(t) = \int_{\mathcal{S}} \nabla\alpha_x[\vec{r}'] \cdot \delta\vec{r}(\vec{r}',t)dm, \quad (2)$$

where ∇ represents the gradient with respect to the change of position of the mass elements dm of the shield $\mathcal{S}$ over which the integral is taken.

[6]This equation was rederived and reworked by the authors to a form that allows for easier computation.

[7]For example, the part of the outer shield directly surrounding the test mass. The general case with multiple structures is a straightforward generalization of the single component case.

Additionally, we can get a rough estimate for the amount of damping required for structural modes in the detection band by assuming independent damping of the normal modes of the structure [18,19].[8] In this case, the normal modes are represented by a set of 'mode shapes' $\{\vec{\psi}_k(\vec{r}')\}$, which are vector fields on the structure that indicate the free vibrational modes of the system. They satisfy the orthogonality condition

$$\langle \psi_k, \psi_l \rangle = \int_{\mathcal{S}} \vec{\psi}_k(\vec{r}') \cdot \vec{\psi}_l(\vec{r}') dm = \tilde{m}_k \delta_{kl}. \tag{3}$$

We have defined the inner product $\tilde{m}_k$ to be the *modal mass* associated with mode k on the structure,[9] δ_{kl} is a Kronecker delta, and the inner product $\langle \cdot, \cdot \rangle$ is defined as an integral over the mass elements of $\mathcal{S}$.

The mode shapes form a complete basis for vector fields defined over the shield surface. In particular, we can decompose the acceleration gradient $\nabla\alpha_x[\vec{r}']$ into a combination of mode shapes,

$$\nabla\alpha_x[\vec{r}'] = \sum_k C_k \vec{\psi}_k(\vec{r}') \quad \text{with} \quad C_k = \frac{\langle \psi_k, \nabla\alpha_x \rangle}{\tilde{m}_k}. \tag{4}$$

Similarly, for the time-varying structural fluctuation $\delta\vec{r}(\vec{r}, t)$,

$$\delta\vec{r}(\vec{r}', t) = \sum_k \delta b_k(t) \vec{\psi}_k(\vec{r}') \quad \text{with} \quad \delta b_k(t) = \frac{\langle \psi_k, \nabla\delta\vec{r}(t) \rangle}{\tilde{m}_k}. \tag{5}$$

The coefficients C_k represent the Newtonian coupling between the axial acceleration of the test mass and the kth mode of the shield. The coefficients b_k will ultimately be related to the modal equations of motion of the structure under the influence of external inputs.

Using the modal basis, we can write the gravitationally-induced axial acceleration, as a function of frequency, as a sum over the individual modes of the shield

$$\delta\hat{a}_x(f) = \sum_k C_k \tilde{m}_k \delta\hat{b}_k(f). \tag{6}$$

The expression for $\delta\hat{b}_k(f)$ can be approximated in terms of the input ground displacement δX_g by considering a one-dimensional harmonic oscillator

$$\delta\hat{b}_k(f) = \left[1 - \frac{f^2}{f^2 - f_k^2 - i\frac{f f_k}{Q_k}}\right] \delta\hat{X}_{g,k}(f), \tag{7}$$

where f_k is the (undamped) natural frequency of mode k and Q_k is its Q-factor. $\delta\hat{X}_{g,k}(f)$ is the projection of the input ground motion into the kth mode of the shield. For lightly damped systems, the resonant frequency is $\tilde{f} \approx f_k$ and the amplification of the input motion on resonance can be approximated directly by the Q-factor; $|\delta\hat{b}_k(\tilde{f})| \approx Q_k |\delta\hat{X}_{g,k}(f_k)|$, with $Q \gg 1$.

IV. DENSITY NEWTONIAN NOISE

One choice for the cooling system designed to bring the test masses' temperature to 124 K is to use the evaporation of liquid nitrogen inside pipes surrounding the outer shield segments. During the liquid-gas transition, the density fluctuations of the nitrogen will alter the local gravitational field around each test mass.

Due to the inherent unpredictability of the boiling process, we will settle for a simplified theoretical approach that will let us set an approximate upper bound for the amount of noise that the density fluctuations can generate on the system in terms of some basic quantities. The model derives key insights from the literature on boiling heat transfer, and focuses on the isolated-bubble regime of nucleate boiling [20]. Much of the discussion presented here is explored in detail in a technical note by the authors [21].

A. Bubbling noise from a single nucleation site

The Newtonian noise model starts by assuming that the overall noise is the quadrature addition of the noise generated by different nucleation sites near the test masses. This model will only be appropriate in the isolated -bubble regime during bubbly flow,[10] but it provides enough insight into the process of nucleation to derive design considerations.

The change in gravitational acceleration between a liquid-filled tube like the one in Fig. 2 due to the presence of a single bubble of volume $V(t)$ is approximately given by

$$a_{x,\text{bubble}}(t) = -(\rho_l - \rho_g) V(t) \alpha_x(\vec{r}(t)), \tag{8}$$

where we have assumed that the bubble is small enough that it can be treated as a point mass. $V(t)$ represents the volume of a single bubble and $\vec{r}(t)$ the position of its center as a function of its lifetime. α_x is the axial acceleration per unit mass, defined in Sec. II C. Note that the net effect of

[8] In this case the structure is said to be *proportionally damped* and it does not represent the vast majority of structures. However, this approach is simple to implement in most FEA packages and it is a good starting point before a more involved analysis.

[9] The choice of normalization for the mode shapes is arbitrary. We utilize a general notation on which the modal masses are explicitly stated in order to draw general conclusions that could be readily applied in simulations.

[10] 'Bubbly flow' is the term used to describe one of the regimes of two-phase flow at low void fractions. It is characterized by a continuous liquid phase with discrete pockets of gas (the bubbles) flowing in it [20].

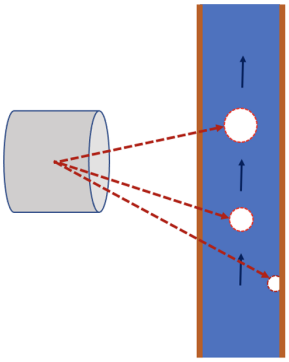

FIG. 2. Simplified depiction of the gravitational interaction between the test mass and bubbles in the liquid nitrogen. We assume all bubbles grow in relevant segments of pipe near the test mass. When bubbles grow and travel, they push away all the liquid (assumed incompressible). The net effect is as if the bubbles had a negative mass compared to the pure liquid.

the bubble is that of a negative mass, since we only care about the difference with respect to the liquid it displaced.

The total acceleration coming from a single nucleation site is just a superposition of the bubbles it produces. Let $\{t_i\}$ represent the set of times at which a new bubble starts growing (or nucleates) in a given nucleation site. This superposition can be approximated by

$$a_{x,\mathrm{site}}(t) = \sum_i a_{x,\mathrm{bubble}}(t - t_i). \tag{9}$$

Owing to the properties of the nucleation cycle, we know that the process is quasiperiodic. The time interval between successive bubble nucleations from the same site $\tau_i = t_{i+1} - t_i$ is roughly regular and can be split into a *waiting time* τ_w and a *growth time* τ_d [20,22]. These concepts, alongside a diagram depicting the nucleation cycle, are shown in Fig. 3.

The nucleation interval is experimentally observed to vary between different nucleating bubbles at the same site, with the variation being a fraction of the waiting time τ_w [23,24]. Following the distribution plotted in Fig. 8 of [24], we model the bubble nucleation intervals for a single site as independent realizations of a gamma-distributed random variable $\tau > 0$. That is,

$$P(\tau_i \in [\tau, \tau + d\tau]) = \rho_1(\tau)d\tau = \frac{1}{\Gamma(k)\theta^k}\tau^{k-1}e^{-\frac{\tau}{\theta}}d\tau. \tag{10}$$

The values of k and θ can be adjusted to match the average nucleation time and its standard deviation.

This model for the acceleration noise generated by the bubbles is called *renewal shot noise* and it is a generalization of the conventional (Poisson) shot noise process. The (single-sided) amplitude spectral density for the fluctuations around the mean of (9) is [25,26]

$$|\delta\hat{a}_{x,\mathrm{site}}(f)| = \sqrt{\frac{2}{\bar{\tau}}}\sqrt{\frac{1 - |\hat{\rho}_1(f)|^2}{|1 - \hat{\rho}_1(f)|^2}}|\delta\hat{a}_{x,\mathrm{bubble}}(f)|. \tag{11}$$

The quantity $1/\bar{\tau} = f_{\mathrm{nuc}}$ is the nucleation frequency of the site, as it is usually defined in the literature on boiling heat transfer. As shown in [21], the spectrum of the renewal shot

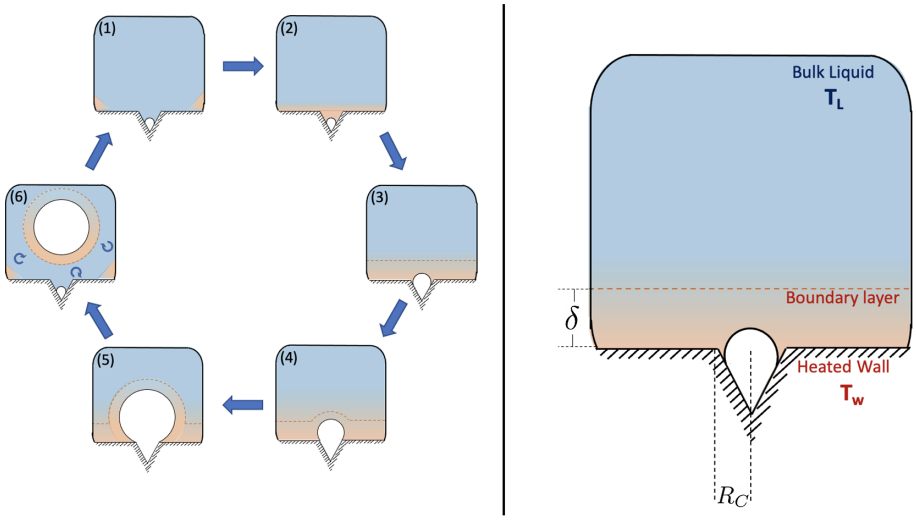

FIG. 3. Simplified depiction of the nucleation cycle. (1) Nucleation starts with vapor trapped in crevices on the heated surface. (2) The heat of the wall starts creating a superheated boundary layer of liquid. (3) The trapped vapor bubble starts growing once the boundary layer is hot enough to support growth against the surface tension. (4) The bubble will continue to grow beyond the size of the cavity, picking up the boundary layer. (5) When the buoyancy of the vapor is enough to overcome the forces attaching the bubble to the surface, the bubble initiates its departure. (6) As the bubble departs from the nucleation site, it disrupts the boundary layer on the wall, cold liquid rushes in on its wake, and the cycle starts anew.

noise exhibits peaks at multiples of the nucleation frequency due to the quasiperiodicity of the nucleation cycle.

The spectral density of the superposition of independent nucleation sites adds in quadrature [27]. Hence, in order to get the aggregate estimate, it is sufficient to compute each nucleation site individually with Eq. (11).

B. Boiling and nucleation

In order to evaluate Eq. (11), we need to populate it with physical parameters coming from the nucleation process. Below, we present key insights from the theory of boiling and nucleation that will aid in our noise analysis, as well as motivating some of the design recommendations at the end of the article.

1. Nucleation site size and density

Nucleation is first possible when the vapor pressure inside a bubble is enough to overcome the surface tension forces of its boundary. The Clausius-Clapeyron relation can be used to determine the minimum size bubble that will not collapse when surrounded by a liquid superheated by an amount ΔT_{sup} [20]

$$R^* = \frac{2\sigma T_{\text{sat}}}{\Delta T_{\text{sup}} \rho_g h_{lg}}, \tag{12}$$

where σ represents the surface tension of the liquid, T_{sat} is the boiling (or saturation) temperature, ρ_g is the gas-phase density, and h_{lg} is the latent heat of evaporation. For bubbles trapped in holes and crevices of a superheated wall, there is the additional constraint that they need to be surrounded by liquid hotter than their inside in order to continue their growth. The interplay between these two effects implies that only a range of crevice sizes $R_{C,\text{max}} \geq R_C \geq R_{C,\text{min}}$ is active given a wall superheat and boundary layer conditions [20,23].

We can estimate the size of the typical active cavity mouth radius R_C by considering the model developed in [23] and selecting the critical radius at which nucleation is first possible for a given wall superheat[11]

$$R_C \approx 2R^* = \frac{4\sigma T_{\text{sat}}}{\Delta T_{\text{sup}} \rho_g h_{lg}}. \tag{13}$$

The number of active nucleation sites can be estimated by using the empirical correlation for the active cavity density found by Zhokhov, referenced in [30]:

$$n = [6.25 \times 10^{-14}\ \text{m}] \left(\frac{2}{R^*}\right)^3. \tag{14}$$

[11]This is similar to the approach used in [28,29]. It is sufficient for an order of magnitude estimate regardless of the specifics of the thermal boundary layer.

2. Bubble lifetime

A nucleating bubble grows in a nucleation site with radius R_C until it reaches a radius large enough to overcome the forces that bind it to the surface. For cryogenic liquids, and neglecting the effect of dynamic forces,[12] the departure radius can be approximated by

$$R_d = \sqrt[3]{\frac{3}{2} \frac{\sigma R_C}{g(\rho_l - \rho_g)}}. \tag{15}$$

For cryogenic liquids and saturated boiling, the growth process of the bubble can be reasonably approximated by considering the Plesset-Zwick solution for the growth of a bubble in a uniformly superheated liquid [32,33]

$$R(t) = \sqrt{\frac{12}{\pi}} \text{Ja} \sqrt{\alpha_l t} = \sqrt{\frac{12}{\pi}} \frac{\rho_l c_{p,l} \Delta T_{\text{sup}}}{h_{lg} \rho_g} \sqrt{\left(\frac{\kappa_l}{\rho_l c_{p,l}}\right) t}, \tag{16}$$

where $\alpha_l = \frac{\kappa_l}{\rho_l c_{p,l}}$ is the thermal diffusivity of the liquid and $\text{Ja} = \frac{\rho_l c_{p,l} \Delta T_{\text{sup}}}{h_{lg} \rho_g}$ is the Jakob number.

Under this approximation, the typical growth time τ_d for the bubble in a nucleation site would be given by

$$\tau_d = \frac{\pi}{12 \alpha_l} \left(\frac{R_d}{\text{Ja}}\right)^2. \tag{17}$$

Finally, under our noninteracting bubble hypothesis, the volume and position for the lifetime of a bubble [both necessary to evaluate Eq. (8)] are given by

$$V(t) = \begin{cases} 0 & \text{for} \quad t < 0 \\ \frac{4}{3}\pi R(t)^3 & \text{for} \quad 0 \leq t \leq \tau_d \\ \frac{4}{3}\pi R_d^3 & \text{for} \quad \tau_d < t, \end{cases} \tag{18}$$

$$\vec{r}(t) = \begin{cases} \vec{r}_0 & \text{for} \quad t \leq \tau_d \\ \vec{r}_0 + \vec{v}(t - \tau_d) & \text{for} \quad \tau_d < t, \end{cases} \tag{19}$$

which correspond to bubbles growing statically at their nucleation sites and getting swept after detachment by the fluid flow, assumed to have velocity $\vec{v}$.[13]

[12]This approach is justified in the case cryogenic liquids on metallic surfaces. The low contact angles ($< 15^o$ as per [31]) make it so that bubbles separate due to breaking with the edge of the nucleation sites where they grow, based on an equilibrium between buoyancy, drag, surface tension and inertial forces [32,33]. Of these forces, only buoyancy and surface tension play a significant role in the heat transfer regime we are considering.

[13]This equivalent to having a slip ratio of 1. This hypothesis can be modified, but it does not impact the qualitative results of this article.

3. Nucleation interval distribution

The interval of time $\bar{\tau}$ needed to nucleate a bubble in a single nucleation site is generally modeled as the sum of the time needed to reestablish a superheated layer (the waiting time τ_w), and the time needed for a nucleating bubble to grow to the departure radius (the growth time τ_d).

We model the waiting time by following [23], where the authors consider the time it takes for the heat of the wall to diffuse and increase the temperature at a distance of $\frac{3}{2}R_C$ away from the wall to the required temperature for bubble growth

$$\tau_w = \frac{1}{\pi\alpha_l}\left(\frac{\frac{3}{2}R_C(T_w - T_l)}{T_w - T_{\text{sat}}(1+\frac{2\sigma}{R_C\rho_g h_{lg}})}\right)^2. \tag{20}$$

As mentioned previously, the nucleation interval is observed to have some variation of the order of a fraction of τ_w [23,24]. To model this effect, we select $k = (\frac{\tau_w+\tau_d}{0.1\tau_w})^2$ and $\theta = \frac{\tau_w+\tau_d}{k}$ in Eq. (10). This corresponds to a mean $\bar{\tau} = \tau_w + \tau_d$ and standard deviation $\sqrt{\bar{\tau^2} - \bar{\tau}^2} = 0.1\tau_w$. These values can be readily substituted in the expression for the Fourier transform of the gamma distribution

$$\hat{\rho}_1(f) = \frac{1}{(1-2\pi i\theta f)^k}. \tag{21}$$

4. Power absorbed

Finally, in order to get an estimate for the Newtonian noise by superimposing different nucleation sites, we need to input the operating superheat of the cryogenic shield in Eqs. (15)–(21). The operating temperature will be a function of the heat load as well as the geometry of the cooling array. Alternatively, it is possible to express the results in terms of the power absorbed by evaporation. The evaporative heat flux $\dot{q}_{\text{evap}}$, is often expressed as [20]

$$\dot{q}_{\text{evap}} = n f_{\text{nuc}} \rho_g V_d h_{lg}, \tag{22}$$

which, when multiplied by the heated area A gives the total heat absorbed by evaporation.

V. RESULTS AND DISCUSSION

A. Tidal Newtonian noise

We focus our attention on the displacement of segment (c) of the outer shield shown in Fig. 1. This section will have the most stringent requirement due to its proximity to the test mass. The dimensions chosen for the outer shield segment are shown in Fig. 4. The shield shown is large enough to fit both the test mass and the penultimate stage of the suspensions. However, as shown in Appendix, changes in the surrounding geometry have little impact on the tidal coupling of the shield at low frequencies.

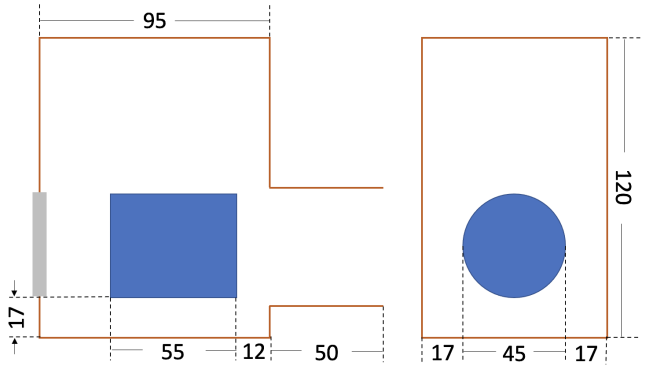

FIG. 4. Dimensions (in cm) for the outer shield utilized for the tidal Newtonian noise estimate in Fig. 5. We assume that the shield is made of copper panels 5 mm thick. The ETM shields have a 1-inch thick sapphire window in the backside of the shield respect to the longitudinal direction, while the ITMs will exhibit two snouts to allow the laser to pass through. This is expanded in Appendix.

For frequencies below the first structural resonance of the outer shield, we can approximate the motion of the outer shield as a pure rigid body motion in phase with the input ground motion. Consequently, the acceleration noise due to longitudinal ground motion can be estimated by

$$|\delta\hat{a}_x(f)| = \left|\int_{\mathcal{S}} \frac{\partial\alpha_x}{\partial x}\, dm\right| |\delta\hat{X}_g(f)|. \tag{23}$$

The results are shown in Fig. 5, with the input motion $|\delta\hat{X}_g(f)|$ taken from 95th percentile ground-motion data from the LIGO Livingston Observatory [34].[14] It can be appreciated that the broadband Newtonian noise coupling is expected to be more than 50 times smaller than the LIGO Voyager design sensitivity at 10 Hz and falling faster than $1/f^3$ in frequency.

Most of the contribution to the Newtonian noise coupling comes from the snout area next to the front and the back of the test mass, due to their proximity to the longitudinal axis.

Therefore, we estimate that the Newtonian noise imposes no extra isolation from ground motion for the outer shields. It is sufficient to connect them directly to their heat sinks. The result from Fig. 5 admits another interpretation; the maximum acceleration input that can be tolerated in the outer shields is about 50 times larger than the 95th percentile ground motion acceleration at LLO at 10 Hz. This sets a Newtonian-noise-imposed limit for the maximum amount of acoustic coupling on the outer shield.

Additionally, we would require enough damping of the structural resonances so they do not contaminate the detection band with Newtonian noise

[14]95th percentile data means that, 95% of the time, the actual amplitude spectrum of the ground motion is lower than the input value utilized in our calculations.

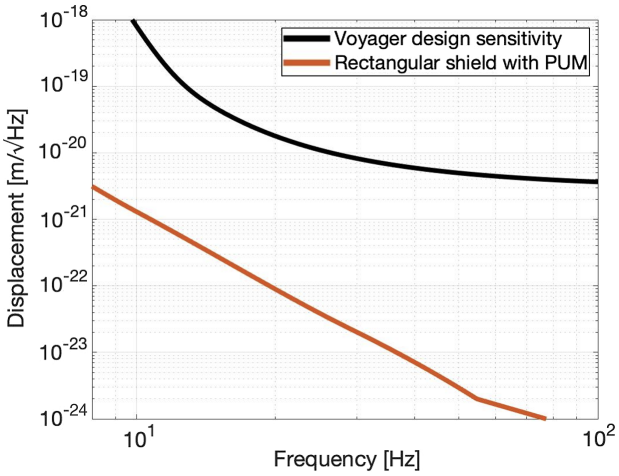

FIG. 5. Tidal Newtonian noise coupling for the general shield geometry from Fig. 4. We consider only rigid-body motion of the outer shield from ground displacement inputs. The input is taken to be the 95th percentile ground motion at the LIGO Livingston Observatory (LLO). The estimate shown adds the contribution of the outer shields from all four test masses in quadrature.

$$(\tilde{m}_k|C_k|)|\delta\hat{X}_{g,k}(f_k)|\frac{Q_k}{(2\pi f_k)^2} < 3\times 10^{21}\ \mathrm{m}/\sqrt{\mathrm{Hz}}. \quad (24)$$

If we estimate $\frac{1}{(2\pi f_k)^2}(\tilde{m}_k|C_k|)|\delta\hat{X}_{g,k}(f_k)|$ to be of the same order of the rigid-body estimate shown in Fig. 5, then damping resonances with frequencies $f_k > 50$ Hz to a Q-factor less than 1000 should be enough to keep the Newtonian noise coupling below the detection band. This level of damping for structural modes should be achievable with a modest amount of engineering.

TABLE I. (Top) Estimated values for physical parameters of nitrogen, taken from [37]. (Bottom) Estimated values for the geometric and engineering parameters of the cryogenic array. Note that, for our estimate, we consider the case of saturated boiling. The geometric variables are defined in Fig. 6.

Symbol	Description	Approximate value
ρ_l	Liquid density	830 kg/m^3
ρ_g	Gas phase density	3 kg/m^3
σ	Surface tension	10^{-2} N/m
$c_{p,l}$	Liquid specific heat	2100 J/kg · K
T_{sat}	Saturation temperature	77 K
h_{lg}	Latent heat of evaporation	2×10^5 J/kg
k_l	Liquid thermal conductivity	0.15 W/m · K
α_l	Liquid thermal diffusivity	8.9×10^{-8} m^2/s
T_l	Liquid bulk temperature	77 K
D	Pipe diameter	0.01 m
L	Individual pipe length	1 m
N_{pipes}	Number of cryogenic pipes	4
d_0	Distance to test mass	0.5 m
v	Flow speed	0.25 m/s

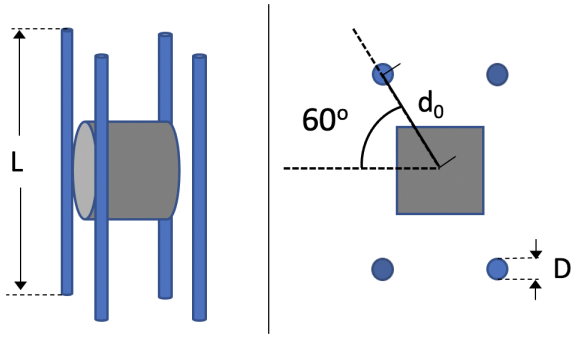

FIG. 6. Geometry of the cryogenic system for the Newtonian noise calculations. The values for each parameter are summarized in Table I. For simplicity, we consider four tubes, all 60 degrees away from the longitudinal direction of the test mass. We also simplify the nucleation sites of each tube to lie in the vertical midpoint of the array, which gives a conservative estimate for the Newtonian noise coupling.

B. Density Newtonian noise

To study this coupling, we evaluate Eqs. (15)–(21), by inputting values for the operating superheat ΔT_{sup} of the outer shield.

Given the design considerations shown in [5], a conservative estimate for the heat load on the outer shield is about 200 W. Consequently, the expected operating superheat ΔT_{sup} will have a value such that the fraction of

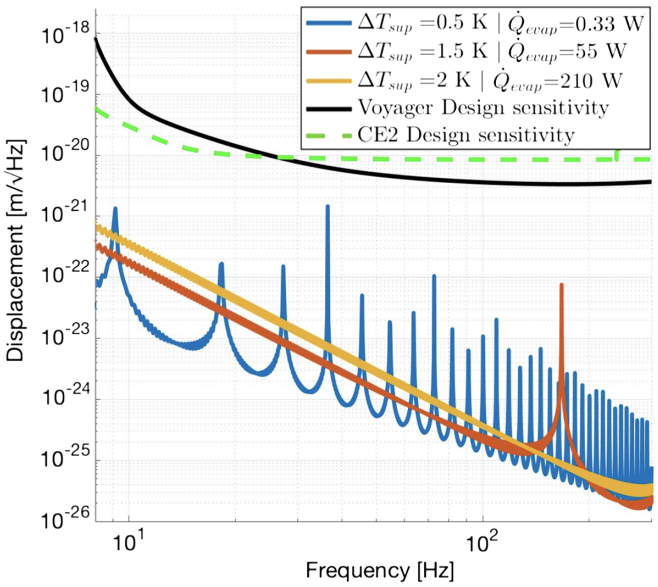

FIG. 7. Estimate of the density Newtonian noise coupling. Three example superheat temperatures are shown, together with their respective estimated evaporative heat transfer per shield. The peaks in the spectrum correspond to the multiples of the nucleation frequencies for each condition (shown in Table II). In this case, we include the LIGO Voyager and CE2 sensitivities in displacement units, where they can be properly compared to the density Newtonian noise, despite the different scaling due to their different baselines.

TABLE II. Calculated values for the nucleation parameters based on Eqs. (15)–(21) and the values of Table I. We evaluate three conditions for the wall superheat (0.5 K, 1.5 K, and 2.0 K) to cover the likely operating range for the cryogenic shield. The values for $\dot{Q}_{\mathrm{evap}}$ are calculated considering the geometry shown in Fig. 6.

Symbol	Description	Calculated values	Units
ΔT_{sup}	Wall superheat	0.5, 1.5, 2.0	K
R_C	Representative cavity radius	8.1, 2.7, 2.0	μm
R_d	Bubble departure radius	0.24, 0.17, 0.15	mm
t_d	Bubble growth time	110, 5.7, 2.7	ms
t_w	Waiting time	2.1, 0.23, 0.13	ms
f_{nuc}	Nucleation frequency	9, 170, 360	Hz
n	Active nucleation site density	0.74, 20, 47	sites/cm^2
$\dot{Q}_{\mathrm{evap}}$	Power absorbed by evaporation	0.33, 55, 210	W

the power absorbed by evaporation $\dot{Q}_{\mathrm{evap}}$ is less than the total heat load of the cooling array.[15] The results of the calculations are shown in Fig. 7 for different values for the outer shield superheat. The approximate values for the physical parameters of nitrogen were taken from [37]. They are summarized in Table I together with a set of estimated values for the geometric factors of the cryogenic shield. It can be immediately noted that the overall value of the density Newtonian noise is expected to be lower than the design sensitivity of the interferometer in the isolated bubble regime for the range of shield superheats tested.

We highlight two important features for the spectra shown in Fig. 7. The Newtonian noise spectra will exhibit peaks in the multiples of the average nucleation frequency f_{nuc}. The magnitude of the peaks depends on the variability on the nucleation time for bubbles, both at the same nucleation site, and at different sites. However, more variability on the nucleation process leads to an increase of the broadband noise for the renewal process, as explained in [25] and discussed in [21].

In principle, these results imply that it is relatively safe to utilize boiling nitrogen (in the bubbly-flow regime) during normal operation of the cryogenic shields from the density Newtonian noise standpoint. However, we note that the periodicity of the nucleation cycle could excite some of the resonant modes of the structure in the case of a coincidence ($f_{\mathrm{struct}} \approx N f_{\mathrm{nuc}}$, for some integer N).

The issue of coincidence could be avoided altogether by utilizing subcooled nitrogen[16] and suppressing nucleation with polished surfaces. A summary of possible boiling suppression strategies is discussed in [21].

The main advantage of a cryogenic system combining subcooled nitrogen with treated surfaces is that it could be tuned to use the boiling heat transfer for the initial cooldown of the interferometer (when high heat transfer capabilities are needed) and single-phase forced convection during steady-state operation (when quiet operation is needed).

VI. CONCLUSIONS

We studied the potential Newtonian noise coupling of double cryogenic arrays to the gravitational-wave channel of next-generation gravitational-wave observatories. This allowed us to set the vibration isolation requirements for the portion of the outer shield surrounding the test masses in LIGO Voyager.

First, we studied the tidal coupling of the shield arrays to the gravitational-wave channel, showing how to project the multipole expansion of the axial acceleration of a cylindrical test mass into the structural modes of the cryogenic shields.

It was determined that the likely coupling from this noise source in the case of LIGO Voyager is low enough that it does not impose any vibration isolation constraints on the outer shields. Additionally, structural resonances above 50 Hz should be damped to a Q-factor of less than 1000 to keep them out of the detection band, which should be within the current engineering abilities of the LIGO collaboration.

Furthermore, we determined that the Newtonian noise coupling sets the requirement for the acoustic coupling to the outer shield to be less than 50 times the observed 95th percentile ground acceleration at 10 Hz. This requirement will be of importance when designing the connection of the heat sinks to the outer shield.

Additionally, the Newtonian noise induced by a phase change on liquid nitrogen near the test masses was also studied. Under some simplifications, we show that this coupling can be modeled by a renewal shot noise process. Qualitatively, it means that it will both exhibit a $1/f^3$ broadband coupling and spectral peaks at multiples of the typical nucleation frequency f_{nuc}. The former one due to the stochastic behavior of nucleation and the latter ones owing to the inherent periodicity of heterogeneous boiling. The amplitude and width of these peaks depends on the variability of the internucleation times, as explained in [21].

We determined that the broadband Newtonian noise created by the phase-change induced density fluctuations is likely to be below the design sensitivity of LIGO Voyager, as well as the second phase of Cosmic Explorer. However, the interplay between the periodicity of nucleation and the structural resonances of the outer shields will need to be considered in the design of the heat sink mechanism for the cryogenic arrays. Our

[15] In the nucleate boiling regime, there are three main mechanisms for heat transfer: forced convection, surface quenching, and evaporation [35,36]. Their relative contribution varies along a heated channel, as the liquid phase temperature and the density of active nucleation sites change.

[16] At one atmosphere, nitrogen can remain in liquid phase down to about 63 K [38]. It is possible to use subcooled liquid nitrogen at 65 K as the coolant for the shield arrays, which should provide enough heat capacity to absorb the heat from the shields without boiling during steady-state operation.

recommendation is to avoid boiling liquid nitrogen during steady-state operation of the observatories. This can be achieved by polishing the surfaces to suppress nucleation and utilizing subcooled nitrogen as the main cooling agent during operation.

We hope that the techniques developed here help drive forward the discussion about the design of the cryogenic part of next-generation gravitational-wave observatories, as well as their integration with the goals of the rest of the subsystems for these instruments.

ACKNOWLEDGMENTS

The authors thank Graeme Eddolls, Pablo Giuliani and Cristina Ceballos for reviewing and providing detailed feedback for this manuscript. This material is based upon work supported by the National Science Foundation under Grant No. 1708006. Any opinions, findings, and conclusions or recommendations expressed in this material are those of the author(s) and do not necessarily reflect the views of the National Science Foundation. O. D. A. thanks MCTI/CNPq for the Grant No. 302841/2017-2.

APPENDIX: GEOMETRIES FOR TIDAL NEWTONIAN NOISE CALCULATIONS

We explored various geometries for the outer shield segment closest to the test mass. In this Appendix we show that, according to our simulations, the expected variability in the rigid-body-displacement Newtonian noise coupling is less than 20%. Similarly, we include insight about the spatial distribution of the coupling over the shield geometry. We conclude that most of the Newtonian noise coupling comes from the snouts in the front and back of the outer shield segment. This information can be used to give a back of the envelope estimate for the Newtonian noise coupling for design purposes.

1. Geometry specifications

Figures 8–10 show the different shield geometries explored for the tidal Newtonian noise calculations aside from the one shown in Fig. 4. They include shields that envelope both the test mass (TST) and penultimate mass (PUM), as well as rounded shields to test whether a higher degree of symmetry would have any impact on the Newtonian noise coupling. Additionally, Fig. 11 shows an example of the two-snout geometry used for the estimated Newtonian noise on the ITMs for every shield design.

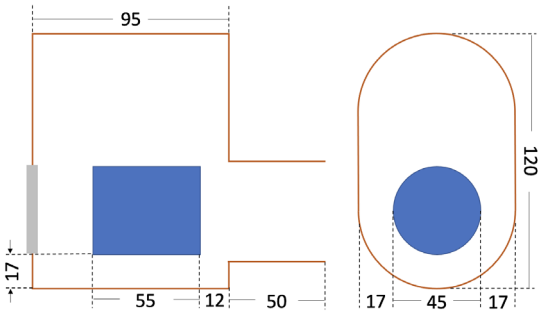

FIG. 8. Side and front views of a rounded-rectangular cross-section ETM outer shield. This particular array would include the penultimate mass (PUM). It has the same characteristics as the one in Fig. 4. Dimensions noted are in cm.

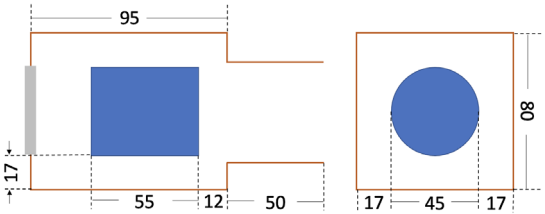

FIG. 9. Side and front views of a rectangular cross-section ETM outer shield. This design considers only test mass cooling, the penultimate mass remains at room temperature. Dimensions are in cm.

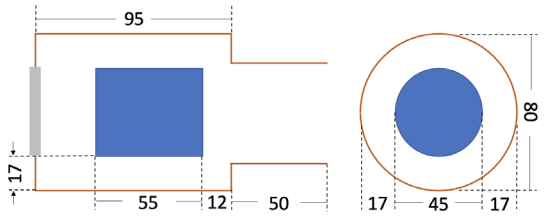

FIG. 10. Side and front views of a circular cross-section ETM outer shield. This design considers only test mass cooling, the penultimate mass remains at room temperature. Dimensions are in cm.

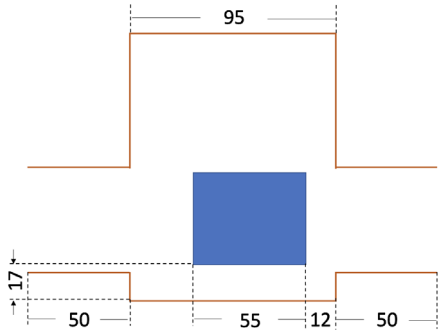

FIG. 11. Side view of an ITM outer shield. Different from the ETM shields from Figs. 8–10, the ITM outer shield has two snouts to allow free passage of the laser light. Dimensions are in cm.

2. Results

For frequencies below the structural modes of the shields, we can assume that the shields move like rigid bodies in phase with the input ground motion. The result for the Newtonian noise coupling is shown in Fig. 13, where

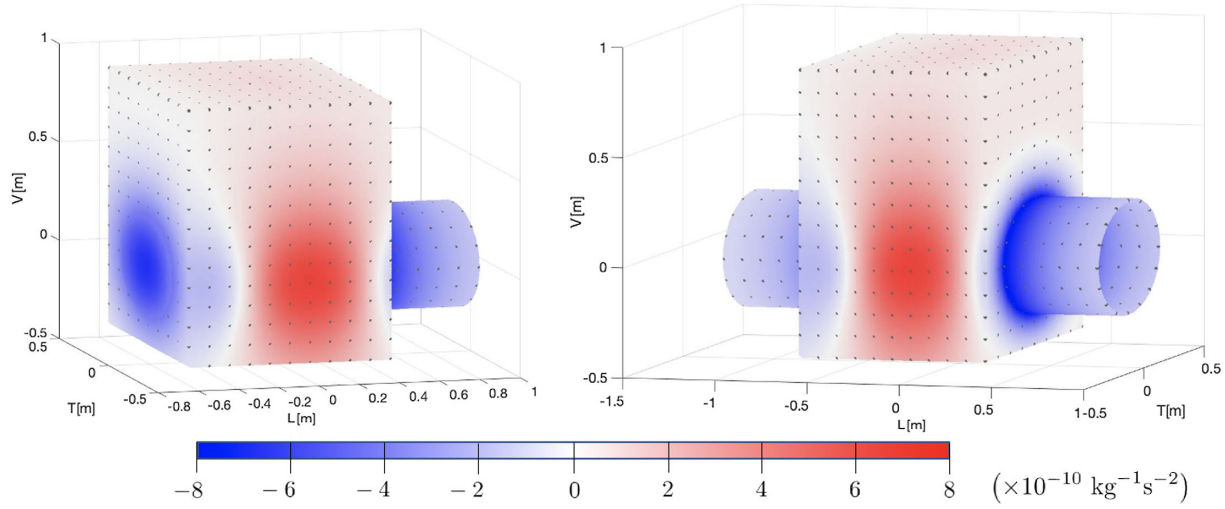

FIG. 12. Projection of the longitudinal acceleration gradient over the surface of the sample geometries for an ETM (left) and an ITM (right). The colors blue and red represent the sign of the gradient coupling per unit mass, while their saturation represents their magnitude.

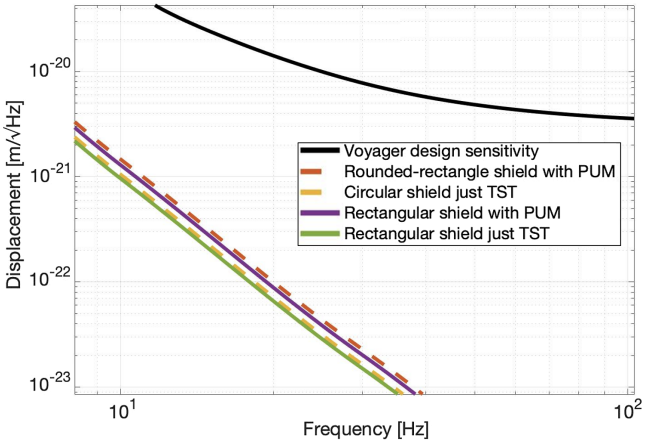

FIG. 13. Comparison of the Newtonian noise coupling for the different shield geometries from Figs. 8–10 with the geometry from Fig. 4. The input motion is 95th percentile ground motion measured in the Livingston Observatory. We add the contributions of all the test masses in quadrature.

we evaluated the longitudinal acceleration gradient directly over the surface of the respective shields according to the equation

$$\frac{\partial \alpha_x}{\partial x} = -G \sum_{n=0}^{\infty} \left[\frac{(2n+2) P_{2n+2}(\cos(\theta))}{r^3} \left(\frac{l}{r}\right)^{2n} \times \sum_{k=0}^{n} C[2n+1, 2k] \frac{P_{2k}(0)}{k+1} \left(\frac{b}{l}\right)^{2k} \right]. \quad \text{(A1)}$$

It can be appreciated in Fig. 13 that the expected Newtonian noise coupling to displacement is of the order of 10^{-21} m/$\sqrt{\text{Hz}}$ at 10 Hz. Moreover, the magnitude of the coupling from the different shield geometries is almost identical, which can be analyzed by observing the projection of the acceleration gradient (A1) over the surface of the shields. An example projection is shown in Fig. 12, where we can appreciate that the portion of the shields that contributes the most to the Newtonian noise coupling are the snouts near the faces of the test mass and the portions of the shield around the barrel. These two areas partially cancel one another, with the snouts having the larger magnitude coupling. The implication is that most of the mass of the shields needed to wrap the PUM has a negligible contribution to the overall level of Newtonian noise. Therefore, it is sensible to approximate the broadband Newtonian noise coupling by only considering the mass of the portions of the shield directly in front of and behind the test mass. With this approximation in mind, we can set the limit of the amount of mass that can be placed in front of (or behind) the test mass by choosing a representative distance of 0.5 m and evaluating Eq. (A1) to find the intersection with the sensitivity curve in displacement units. The mass in the case of LIGO Voyager is about 200 kg. This estimate is also valid for the case of CE2.

[1] B. P. Abbott, R. Abbott, T. Abbott, M. Abernathy, F. Acernese, K. Ackley, C. Adams, T. Adams, P. Addesso, R. Adhikari *et al.*, Phys. Rev. Lett. **116**, 061102 (2016).

[2] B. P. Abbott, R. Abbott, T. Abbott, F. Acernese, K. Ackley, C. Adams, T. Adams, P. Addesso, R. Adhikari, V. Adya *et al.*, Phys. Rev. Lett. **119**, 161101 (2017).

[3] B. P. Abbott, S. Bloemen, P. Canizares, H. Falcke, R. Fender, S. Ghosh, P. Groot, T. Hinderer, J. Hörandel, P. Jonker *et al.*, Astrophys. J. Lett. **848**, L12 (2017).

[4] J. Miller, L. Barsotti, S. Vitale, P. Fritschel, M. Evans, and D. Sigg, Phys. Rev. D **91**, 062005 (2015).

[5] R. X. Adhikari, K. Arai, A. Brooks, C. Wipf, O. Aguiar, P. Altin, B. Barr, L. Barsotti, R. Bassiri, A. Bell *et al.*, Classical Quant. Grav. **37**, 165003 (2020).

[6] Virgo Collaboration, Advanced Virgo plus phase I-design report, Virgo Technical Report No. VIR-0596A-19, 2019, https://tds.virgo-gw.eu/ql/?c=14430.

[7] M. Punturo, M. Abernathy, F. Acernese, B. Allen, N. Andersson, K. Arun, F. Barone, B. Barr, M. Barsuglia, M. Beker *et al.*, Classical Quant. Grav. **27**, 194002 (2010).

[8] D. Reitze, R. X. Adhikari, S. Ballmer, B. Barish, L. Barsotti, G. Billingsley, D. A. Brown, Y. Chen, D. Coyne, R. Eisenstein *et al.*, Bull. Am. Astron. Soc. **51**, 035 (2019), arXiv:1907.04833.

[9] K. Ackley, V. Adya, P. Agrawal, P. Altin, G. Ashton, M. Bailes, E. Baltinas, A. Barbuio, D. Beniwal, C. Blair *et al.*, Pub. Astron. Soc. Aust. **37** (2020).

[10] T. Middelmann, A. Walkov, G. Bartl, and R. Schödel, Phys. Rev. B **92**, 174113 (2015).

[11] K. Somiya, Classical Quant. Grav. **29**, 124007 (2012).

[12] B. Shapiro, R. X. Adhikari, O. Aguiar, E. Bonilla, D. Fan, L. Gan, I. Gomez, S. Khandelwal, B. Lantz, T. MacDonald *et al.*, Cryogenics **81**, 83 (2017).

[13] P. R. Saulson, *Fundamentals of Interferometric Gravitational Wave Detectors* (World Scientific, Singapore, 1994), 10.1142/2410.

[14] T. Creighton, Classical Quant. Grav. **25**, 125011 (2008).

[15] A. Nishizawa, *KAGRA Detector Characterization Meeting 2016* (2016), http://gwwiki.icrr.u-tokyo.ac.jp/JGWwiki/KAGRA/Subgroups/DET/Meet/Agenda20161129.

[16] J. Harms, Living Rev. Relativity **18**, 3 (2015).

[17] N. Lockerbie, A. Veryaskin, and X. Xu, Classical Quant. Grav. **10**, 2419 (1993).

[18] B. Yang, *Stress, Strain, and Structural Dynamics: An Interactive Handbook of Formulas, Solutions, and MATLAB Toolboxes* (Academic Press, New York, 2005).

[19] W. K. Blake, Chapter 5 - Fundamentals of flow-induced vibration and noise, *Mechanics of Flow-Induced Sound and Vibration, Volume 1: General Concepts and Elementary Sources*, 2nd ed. (Academic Press, New York, 2017), pp. 323–410, 10.1016/B978-0-12-809273-6.00005-1.

[20] S. M. Ghiaasiaan, *Two-Phase Flow, Boiling, and Condensation: In Conventional and Miniature Systems* (Cambridge University Press, Cambridge, England, 2007), 10.1017/CBO9780511619410.

[21] E. Bonilla, LIGO Document No. LIGO-T1600475, 2016, https://dcc.ligo.org/LIGO-T1600475-v4/public.

[22] L. S. Tong and Yu. S. Tang, *Boiling Heat Transfer and Two-Phase Flow*, 2nd ed. (CRC Press, Boca Raton, Florida, USA, 1997), 10.1201/9781315138510.

[23] H. Chi-Yeh and P. Griffith, Int. J. Heat Mass Transfer **8**, 905 (1965).

[24] D. Euh, B. Ozar, T. Hibiki, M. Ishii, and C.-H. Song, J. Nucl. Sci. Technol. **47**, 608 (2010).

[25] M. S. Bartlett, J. R. Stat. Soc. Ser. B **25**, 264 (1963).

[26] B. Lindner, A brief introduction to some simple stochastic processes, *Stochastic Methods in Neuroscience*, edited by C. Laing and G. J. Lord (Oxford University Press, New York, 2009), pp. 1–28, 10.1093/acprof:oso/9780199235070.003.0001.

[27] B. Lindner, Phys. Rev. E **73**, 022901 (2006).

[28] Y. A. Kirichenko and N. Levchenko, J. Appl. Mech. Tech. Phys. **17**, 538 (1976).

[29] Yu. A. Kirichenko, M. L. Dolgoi, N. M. Levchenko, V. V. Tsybulskii, L. A. Slobozhanin, and N. S. Shcherbakova, A study of the boiling of cryogenic liquids, *Heat Transfer: Soviet Research*, edited by J. P. Hartnett, T. F. Irvine, and N. Zuber (Scripta Technica, Inc., 1976), Vol. 8, pp. 63–72, https://inis.iaea.org/search/search.aspx?orig_q=RN:9391993.

[30] V. Borishanskii and K. Zhokhov, J. Eng. Phys. **15**, 932 (1968).

[31] P. Brennan and E. Skrabek, NASA Report No. CR-121939, 1971.

[32] W. Bald, Cryogenics **13**, 457 (1973).

[33] Y. A. Kirichenko, J. Eng. Phys. **25**, 811 (1973).

[34] J. Harms, LIGO Document No. LIGO-T1500224, 2015, https://dcc.ligo.org/LIGO-T1500224/public.

[35] R. L. Judd and K. S. Hwang, J. Heat Transfer **98**, 623 (1976).

[36] X. Li, W. Wei, R. Wang, and Y. Shi, Int. J. Heat Mass Transfer **52**, 1510 (2009).

[37] J. Jensen, R. G. Stewart, W. Tuttle, H. Brechna, and A. Prodell, *Brookhaven National Laboratory Selected Cryogenic Data Notebook: Section VI. Properties of Nitrogen* (Brookhaven National Laboratory, Upton, NY, USA, 1980).

[38] V. Cheng, W. Daniels, and R. Crawford, Phys. Rev. B **11**, 3972 (1975).